An Active Clamp Flyback Converter With High Precision Primary-Side Regulation Strategy

Cheng-Yu Tang, *Member, IEEE*, Wei-Zhen Lin, and Yu-Ching Tan

***Abstract*—The active clamp flyback (ACF) converter has been widely adopted because of the feature of isolation, soft-switching, and high conversion efficiency. On the other hand, due to the characteristic of the circuit cost reduction and the fast control response, the primary-side regulation (PSR) has become a popular control method for isolated power converters. However, high precision PSR strategies for ACF converters are not exposed. Therefore, the aim of this article is to propose a high precision PSR strategy for the ACF converter. Relations between the primary-side current and the secondary-side current are analyzed and derived. Both of the continuous conduction mode operation and the discontinuous conduction mode operation will be considered. The output voltage control mode or the output current control mode can be selected via the proposed strategy. In addition, a secondary-side losses compensation (SSLC) strategy is developed to deal with the non-ideal circuit characteristics as well as to enhance the control accuracy. Operational principles and thorough mathematical derivations will also be revealed. Finally, both simulation and experimental results obtained from a 100 W prototype circuit demonstrate the performance and feasibility of the proposed PSR and SSLC strategy. Validations show that the control accuracy of the output voltage and the output current are 98.54% and 98.42%, respectively.**

***Index Terms*—Active clamp flyback converter (AFC), high precision control, primary-side regulation (PSR).**

I. Introduction

NOWADAYS, power electronics have become necessary technologies for electrical energy conversion, renewable energy systems and advanced consumer electronics. For energy saving and carbon reduction, high conversion efficiency is an essential criteria for power converters [1]–[3]. Due to the simple circuit structure and the feature of isolation, the flyback converter has become one of the most commonly used topologies for low power applications [4]–[7]. Besides, in order to reduce the power loss as well as to increase the efficiency, the active clamp topology have been adopted for the flyback converter [8]–[10]. With the soft-switching characteristics, the efficiency of the active clamp flyback (ACF) converter can be improved.

Traditionally, the secondary-side-regulation (SSR) is adopted for the flyback converter. The output voltage or current signal on the secondary-side should be sensed, whereas the controller on the primary-side generates the pulsewidth modulation signal. In order to isolate the signal between the primary-side and the secondary-side of the transformer, an optocoupler should be included. However, the circuit cost will be increased while the transient response might be decreased with the optocoupler. In order to reduce the circuit cost and standby power losses, primary-side control methods for flyback converter were presented in [11]–[18]. With the PSR, only electric signals of the primary-side will be measured and estimated. Therefore, the output voltage or current can be controlled without the optocoupler. In addition, the precise primary-side current measurement is also important for the PSR control [19], [20]. Wu *et al.* [19] proposed a slope detection of the primary-side current to estimate the actual primary-side peak current. Compare to the conventional linear slope compensation methods, the proposed one can correct the peak current measuring error caused by the propagation delay time. In [20], a kind of average inductor current measure and control strategy for multimode was introduced. The average inductor current measurement strategy is based on the Miller stage to recognize the state of the MOSFET, which eliminates the error caused by the MOSFET. The average current of primary inductor is obtained and there is no need to estimate the rising slope and the peak value of the inductor current. Moreover, the utilization of the auxiliary winding could be considered to realize the PSR. Xu *et al.* [21] revealed that there will be sampling errors of the sampled output voltage from auxiliary winding in PSR flyback converter. To improve the constant voltage accuracy, a novel digital controlled sampling strategy is proposed. This scheme uses a digital ramp sampling method to sample output voltage. If the battery is connected to the output of the ACF, both of the output voltage and current control should be considered to achieve the CC-CV charging control, as mentioned in ref [22]. In [22], a novel ring detection and demagnetization portion control technique is proposed, with which the ending time of demagnetization can be accurately determined and the portion of demagnetization in switching periods remain precisely the same, which enable the accuracy of constant current output. In the PD fast charging and LED driving applications, both of the output voltage and current control are also necessary.

Manuscript received August 27, 2021; revised January 8, 2022; accepted February 18, 2022. Date of publication March 29, 2022; date of current version May 23, 2022. This work was supported by the Ministry of Science and Technology of Taiwan, under Grant MOST 109-2221-E-027-050-MY2. Recommended for publication by Associate Editor G. Moschopoulos. *(Corresponding author: Cheng-Yu Tang.)*

Cheng-Yu Tang and Yu-Ching Tan are with the Renewable Energy and Power Conversion Laboratory, Department of Electrical Engineering, National Taipei University of Technology, Taipei 10608, Taiwan (e-mail: cytang@ntut.edu.tw; nina878418@gmail.com).

Wei-Zhen Lin is with Delta Electronics, Taoyuan 320023, Taiwan (e-mail: brian.wz.lin@deltaww.com).

Color versions of one or more figures in this article are available at https://doi.org/10.1109/TPEL.2022.3162960.

Digital Object Identifier 10.1109/TPEL.2022.3162960

Although these methods are effective, they can only be adopted for the conventional flyback converter or the quasi-resonant flyback (QRF) converter. However, our work focuses on the ACF converter. The circuit topology, circuit features, operational principles and theoretical waveforms between QRF and the ACF are different. That is to say, the proposed PSR methods in these literatures cannot by adopted for the ACF. Therefore, the authors developed a PSR strategy, which is utilized for the ACF. In addition, there is no need to sense the voltage signal from the auxiliary winding in our work. Besides, with the proposed circuit and proposed control strategy, complex compensating circuits are not required in the control loop. The control algorithm and compensators can be realized in the main controller. Besides, there is no need to add the optocoupler, which is a necessary component with SSR. Therefore, compare to conventional circuit and control, the circuit cost and size can be reduced with the proposed circuit and strategy.

On the other hand, non-ideal characteristics exist in the secondary-side of the circuit. When the secondary-side diode is conducted, a part of losses will be generated by the unavoidable diode forward voltage (V_F). The diode conduction loss not only reduces the circuit efficiency, but also decreases the output voltage and current. Unfortunately, conventional PSR methods only utilize the electric information of the primary-side. Effect of the secondary-side losses might not be taken into account. As a result, the output voltage and current error will be increased while the control accuracy will be decreased.

Therefore, main aims of this article can be summarized as follows.

1) A PSR strategy for the ACF converter is proposed.
2) Both of the continuous conduction mode (CCM) and the discontinuous conduction mode (DCM) operation will be considered and analyzed.
3) A secondary-side loss compensation (SSLC) is developed to enhance the control accuracy.

Detailed circuit operations, theoretical analysis and mathematical derivations of the proposed PSR and SSLC will be presented. Finally, simulation and experimental results obtained from a 100W prototype circuit verify the performance of the proposed control strategy.

II. Circuit Configuration and Proposed Control Strategies

A. Circuit Configurations of the ACF Converter

Fig. 1 shows the circuit diagram of the ACF with the proposed PSR strategy. According to Fig. 1, the main power stage is composed of the main switch Q_1, the auxiliary switch Q_2, the active clamp capacitor $C_{\rm Clamp}$, the magnetizing inductance L_m, the resonant inductance L_r, the output diode D_o, the output capacitor C_o, and the load resistance R_L. Besides, the digital signal processor (DSP) TMS320F28379D is utilized as the circuit controller. In order to simplify the analysis, all elements are considered as ideal except the parasitic capacitors, C_1 and C_2.

It is worth mentioning that with the proposed strategy, the resonant inductor current i_{Lr} will be utilized to achieve the proposed PSR strategy. Therefore, a resistor R_{Lr} is connected in series with the resonant inductor, as shown in Fig. 1. The purpose of R_{Lr} is to sense the resonant inductor current i_{Lr} and convert it to the voltage signal. Besides, the primary-side transformer voltage V_p should be sensed. Detailed analysis of the proposed PSR concept will be presented in the next section.

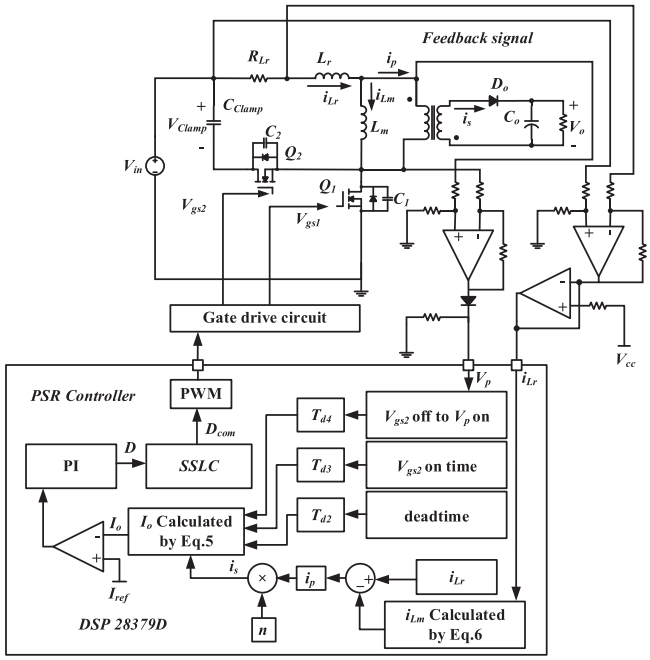

Fig. 1. Circuit diagram of the ACF with the proposed PSR strategy.

B. Proposed Primary-Side Regulation Strategy

In this section, the proposed PSR strategy will be described in detailed. First, theoretical waveforms of the ACF converter operated in CCM and DCM are shown in Fig. 2(a) and (b), respectively. It can be confirmed that the main difference between the CCM and DCM is the of the magnetizing inductor current. However, the proposed PSR strategy can be adopted for both CCM and DCM operation.

In the following, the CCM operation is first considered. Theoretical waveforms of the ACF converter operated in CCM are shown in Fig. 2(a). From Fig. 2(a), C_1 is charged to $V_{\rm in}+nV_o$ at t_2, whereas C_2 will be discharged to 0V. Therefore, the auxiliary switch, Q_2, is able to achieve the zero voltage switching (ZVS) turn-ON. On the other hand, at t_6, C_2 is charged to $V_{\rm in}+nV_o$, whereas C_1 will be discharged to 0V. Therefore, the main switch, Q_1, can achieve the ZVS turn-ON. From Fig. 2(a), it can be seen that I_o is equal to the effective value of the average secondary-side current $i_s(t)$. Therefore, I_o can be calculated by the area of $i_s(t)$, as

$$I_o = \frac{1}{T_s}\int_0^{T_s} i_s\,(t)\,dt \tag{1}$$

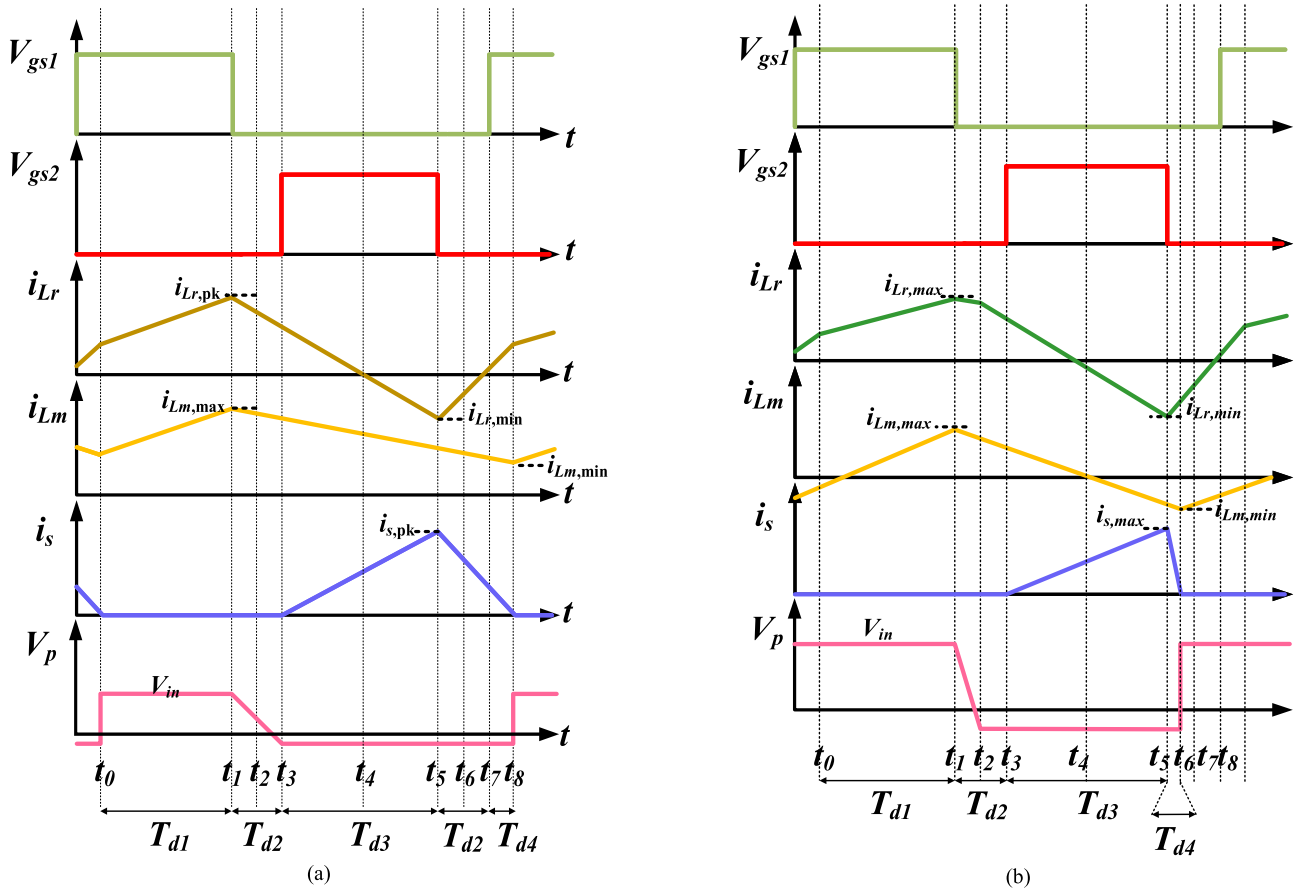

Fig. 2. Theoretical waveforms of the ACF converter. (a) CCM operation. (b) DCM operation.

where T_s is the switching period. In addition, the relation between the primary-side current, i_p, and $i_s(t)$ can be written as

$$i_s(t) = n \times i_p \tag{2}$$

where n is the transformer turns ratio. From Fig. 1, it can be confirmed that $i_p(t)$ will be equal to the difference between $i_{Lr}(t)$ and the magnetizing inductor current $i_{Lm}(t)$ as

$$i_p(t) = i_{Lr}(t) - i_{Lm}(t). \tag{3}$$

After the rearrangement of (2) and (3), $i_s(t)$ can be expressed as

$$i_s(t) = n \times i_p = n\left[i_{Lr}(t) - i_{Lm}(t)\right]. \tag{4}$$

With the combination of (1) and (4), I_o can be derived as:

$$I_o = \left| \frac{1}{T_s} \times \frac{1}{2} \left\{ (T_{d2} + T_{d3} + T_{d4}) \times n \left[i_{Lr}(t_5) - i_{Lm}(t_5) \right] \right\} \right| \tag{5}$$

where T_{d2} is the deadtime between Q_1 and Q_2, as the interval between t_1 and t_3 shown in Fig. 2(a). T_{d3} is the on-time of V_{gs2}, as the interval between t_3 and t_5. T_{d4} is the interval between t_7 and t_8. It is worth mentioning that in to (3)–(5), the value of i_{Lr} can be obtained via the R_{Lr}.

In (5), due to the fact that i_{Lm} cannot directly be obtained, i_{Lm} at t_5 should be estimated and calculated by

$$i_{Lm}(t_5) = i_{Lm,\max} - \frac{\Delta i_{Lm} \times (T_{d2}+T_{d3})}{\left(\frac{3}{2}T_{d2} + T_{d3} + T_{d4}\right)} \tag{6}$$

where $i_{Lm,\max}$ is the maximum magnetizing inductor current, and it will approximately be equal to the maximum resonant inductor current, $i_{Lr,\max}$, at t_2, as shown in (7). Besides, Δi_{Lm} is the magnetizing inductor current variation, which can be obtained as

$$i_{Lm,\max} \approx i_{Lr,\max}. \tag{7}$$

$$\Delta i_{Lm} = \frac{V_p \times D \times T_s}{L_m} \tag{8}$$

where D is the duty cycle of Q_1, which can be calculated from the ACF voltage transfer function shown in (9). Besides, V_p is the primary-side voltage of the transformer, which can be obtained by (10)

$$V_o = V_{in} \times \frac{1}{n} \times \frac{D}{1-D} \tag{9}$$

$$V_p = \frac{V_{in} \times L_m}{L_m + L_r} \tag{10}$$

where V_{in} and V_o are the input and output voltage, respectively.

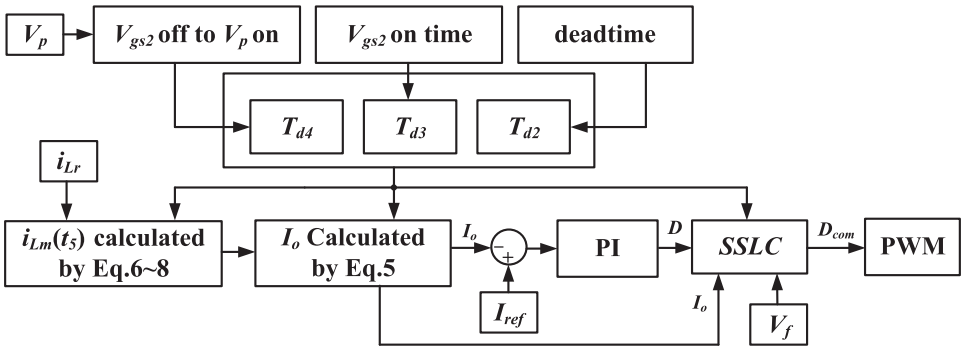

Fig. 3. Control block diagram of the proposed PSR.

On the other hand, the proposed PSR strategy can also be adopted for the DCM operation. Theoretical waveforms of the ACF converter operated in DCM are shown in Fig. 2(b). Under the DCM operation, i_{Lm} will be discontinuous. The conducting period of the output diode will be different in CCM and DCM. Therefore, with the consideration of the DCM operation, Eq. (5) should be modified as

$$I_o = \left| \frac{1}{T_s} \times \frac{1}{2} \left\{ (T_{d3} + T_{d4}) \times n \left[i_{Lr}(t_5) - i_{Lm}(t_5) \right] \right\} \right|. \tag{11}$$

After comparing (5) and (11), it can be confirmed that the only difference between the CCM and the DCM is the diode conducting period. The basic concept and derivation processes of the proposed PSR will be the same under both CCM and DCM operation.

C. Secondary-Side Losses Compensation

The proposed PRC strategy can effectively be adopted for the ACF converter. However, with PSR methods, only the primary-side current is considered and controlled. Unfortunately, nonideal characteristics of the secondary-side parameters might decrease the PSR control accuracy. Therefore, in order to increase the accuracy as well as to decrease the error, an SSLC is developed in this article. With the proposed SSLC, power loss of the secondary-side diode will be considered and analyzed. Consequently, the output voltage and current accuracy can be increased via the SSLC. Fig. 3 is constructed to further illustrate the control block diagram of the proposed PSR and the implementation of the SSLC.

In the following, losses of the diode will be analyzed. First, the average current on the diode can be expressed as

$$i_{s,\text{rms}} = \frac{2 \times I_o}{\sqrt{3 \times T_{d,\text{on}}}} \tag{12}$$

where I_o is the output current obtained from (5) or (11). $T_{d,\text{on}}$ is the diode conducting period.

Because that $T_{d,\text{on}}$ is equal to $T_{d2} + T_{d3} + T_{d4}$, Equation (12) can be modified as:

$$i_{s,\text{rms}} = \frac{2 \times I_o}{\sqrt{3 \times (T_{d2} + T_{d3} + T_{d4})}}. \tag{13}$$

The diode power loss, $P_{\text{Diode,loss}}$, can be calculated by

$$P_{\text{Diode,loss}} = i_{s,\text{rms}} \times V_F \tag{14}$$

where V_F is the diode forward voltage. With the combination of (13) and (14), $P_{\text{Diode,loss}}$ can be written as

$$P_{\text{Diode,loss}} = \frac{2 \times I_o}{\sqrt{3 \times (T_{d2} + T_{d3} + T_{d4})}} \times V_F. \tag{15}$$

From (14), it can be confirmed that $P_{\text{Diode,loss}}$ will be increased if the output current is increased. Consequently, the output voltage will be reduced. As a result, the control accuracy will be decreased. In order to deal with this issue, the SSLC strategy is developed. With the SSLC, a compensating voltage V_{com} is derived from the power loss of the diode and the output current as

$$V_{\text{com}} = \frac{P_{\text{Diode,loss}}}{I_o}. \tag{16}$$

After combining (9) and (16), a compensating duty cycle D_{com} can be obtained, as shown

$$D_{\text{com}} = \frac{1}{\frac{V_{\text{in}}}{V_{\text{com}} \times n} + 1}. \tag{17}$$

Eventually, the output voltage and current can be compensated, whereas the control accuracy will be improved via the consideration of V_{com} and D_{com}.

It is worth mentioning that the ZVS function is independent with the developed SSLC. The ZVS condition can be determined by the leakage inductance, the parasitic capacitances and the deadtime period. The secondary-side losses will not affect the performance of ZVS.

III. Simulation and Experimental Results

In order to verify the proposed PSR strategy, both of the simulation and experiment results will be demonstrated in this section. Specifications of the prototype circuit are given in Table I. The rated power is 100 W. Considering that the input voltage of the ACF converter will be fixed via the frond-end PFC, the input voltage is set as 400 V. The output voltage is set as 48 V. The magnetizing and leakage inductance are 2.6 mH and 33 μH, respectively. The switching frequency is determined as 100 kHz. The MOSFET, FQPF9N90CT, is chosen as the main

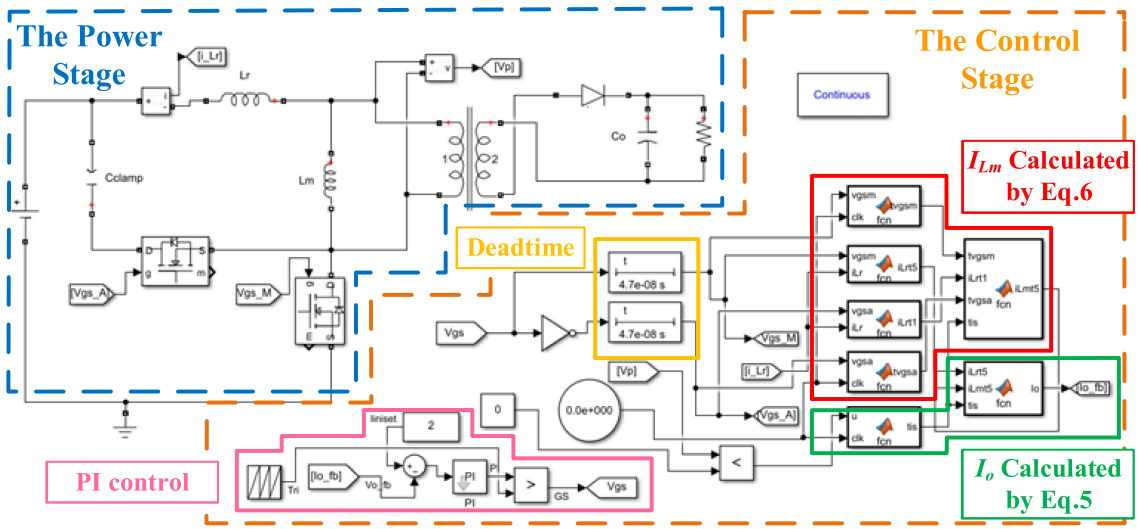

Fig. 4. The circuit diagram of the ACF converter with the proposed PSR strategy on MATLAB/Simulink.

TABLE I
SPECIFICATIONS OF THE PROTOTYPE ACF CONVERTER

Parameters	Value or type
Rated power (P_o)	100W
Input voltage (V_{in})	400V
Input current (I_{in})	0.25A
Output voltage (V_o)	48V
Output current (I_o)	6.083A
Magnetizing inductance (L_m)	2.76mH
Leakage inductance (L_k)	33μH
Turns ratio (N_p/N_s)	4.08
Switching frequency (f_s)	100kHz
Output capacitance (C_o)	470μF/100V
Main switches of Q_1 and Q_2	FQPF9N90CT
System controller	DSP TMS320F28379D

circuit switches. The DSP, TMS320F28379D is selected as the main system controller. It should be mentioned that the Cgd of FQPF9N90CT is only 14 pF. Besides, the switching frequency is set as 100 kHz in this work. Therefore, the turn OFF losses is not significant. On the other hand, because of the ZVS feature of the ACF converter, the turn ON losses could be neglected. Besides, the Adc conversion rate of TMS320F28379D is 3.5 MSPS. With the proposed method, the peak current of the resonant inductor should be measured. But, higher MCU operating frequency will decrease the number of sampling points. Unfortunately, few sampling points might reduce the control accuracy. In the future, the proposed PSR strategy could be realized and implemented in the ASIC, whereas the switching frequency can be decreased with the ASIC.

A. Simulation Results

The circuit diagram of the ACF converter with the proposed PSR strategy on MATLAB/Simulink is shown in Fig. 4. Simulation waveforms of the gate-to-source voltage V_{gs1} the drain-to-source voltage V_{ds1} the primary-side voltage of the transformer V_p the time interval, T_{d2}, T_{d3}, and T_{d4} are shown in Fig. 5 It can be seen that V_{ds1} reduces to 0V before V_{gs1} is turned ON. In other words, the ZVS feature can be achieved. Besides, simulation waveforms of i_{Lr} and i_s are shown in Fig. 5(d). With the proposed PSR strategy i_{Lr} will be sensed and controlled. Eventually, I_o can be calculated as 1.925A from the simulation results, which is close to the theoretical I_o value, 1.917A. On the other hand, simulation waveforms of the proposed ACF converter under the DCM operation are shown in Fig. 6. It can be confirmed that the simulation results match the theoretical waveforms.

B. Experimental Verification

The prototype circuit figure of the proposed ACF converter is shown in Fig. 7. It can be seen that the prototype circuit consists of the ACP main power stage and the DSP control stage. In the experimental setup, the dc source, EA PSI-9750-12, is connected to the input port of the ACF. The dc load, Chroma 63202A, is connected to the output port. With the implemented circuit and proposed control strategy, complex compensating circuits are not required in the control loop. The control algorithm and compensators can be realized in the main controller. Besides, there is no need to add the optocoupler, which is a necessary component with SSR. Therefore, compare to conventional circuit and control, the circuit cost and size can be reduced with the proposed circuit and strategy. In addition, the proposed PSR strategy could be implemented in the ASIC in the future. Therefore, the controller cost can be decreased.

Fig. 8 shows experimental results of the proposed PSRACF under the CCM mode and the full load operation. Waveforms of V_{gs1}, V_{gs2}, T_{d2}, and T_{d3} are shown in Fig. 8(a) and (b).

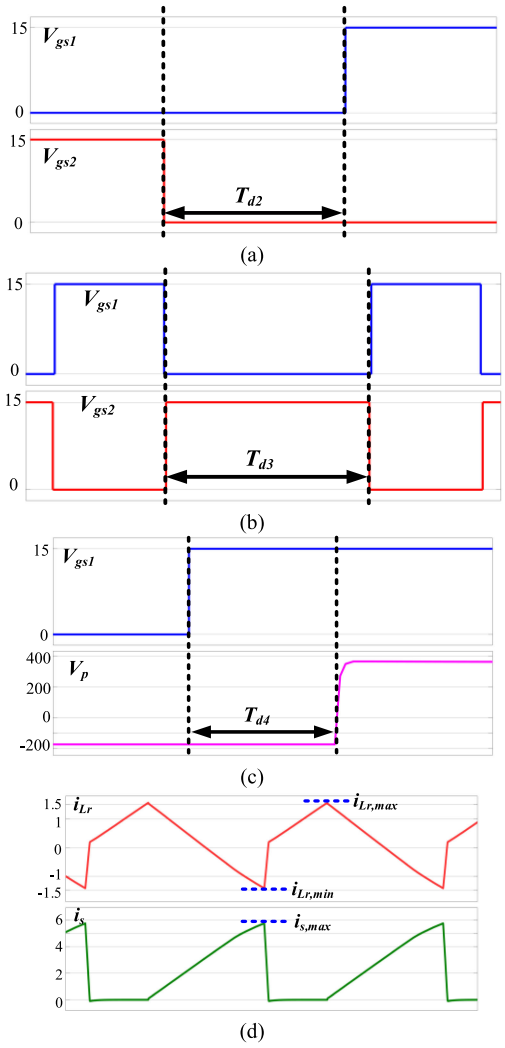

Fig. 5. Simulation waveforms of the proposed ACF converter under the CCM operation. (a) V_{gs1}, V_{gs2}, and T_{d2}. (b) V_{gs1}, V_{gs2}, and T_{d3}. (c) V_{gs1}, V_p, and T_{d4}. (d) i_{Lr} and i_s.

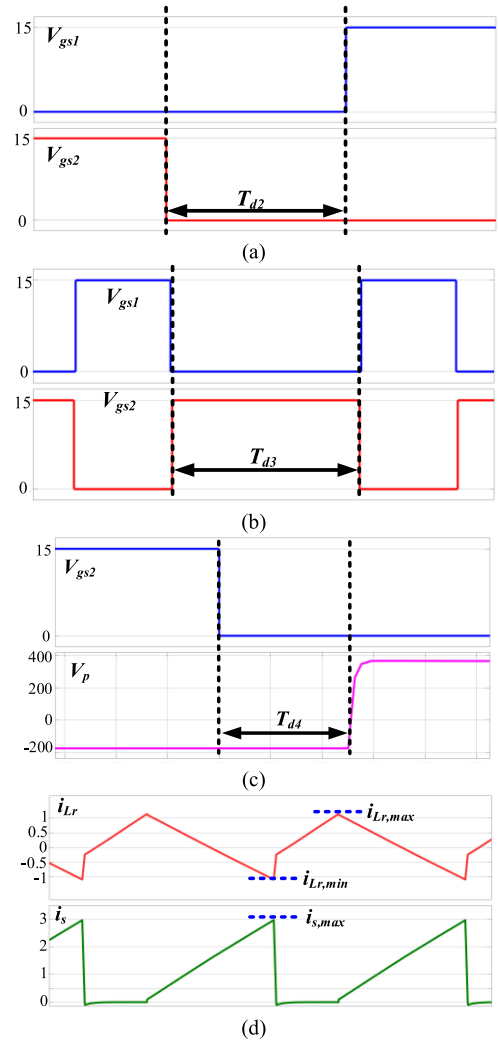

Fig. 6. Simulation waveforms of the proposed ACF converter under the DCM operation. (a) V_{gs1}, V_{gs2}, and T_{d2}. (b) V_{gs1}, V_{gs2}, and T_{d3}. (c) V_{gs1}, V_p, and T_{d4}. (d) i_{Lr} and i_s.

Waveforms of V_{gs1}, V_p, and T_{d4} are shown in Fig. 8(c). It is worth mentioning that T_{d2}, T_{d3}, and T_{d4} can be calculated as 280 ns, 6.015 μs and 40 ns, respectively. It should be noticed that traditionally, there would be noises in the output of the sampling signal, which might be caused by the leakage inductance or circuit nonideal characteristics. In our work, the primary-side voltage V_p is only utilized to detect the zero-crossing point, whereas there is no need to use the sensed value of V_p in the proposed PSR calculation process. On the other hand, with proper PCB layout and the utilization of the sandwich (interleaved) winding of the transformer, the noise can effectively be reduced. In Fig. 8(c), it can be confirmed that the zero-crossing point is not affected by any noises. Waveforms of i_{Lr} and i_s are shown in Fig. 8(d). The maximum and minimum resonant inductor current can be measured as 1.63 and -1.26A, respectively. With the combination of these experimental values and (5), I_o can be calculated as 2.05A. Compare to the theoretical I_o value under the full load, the error is only 1.6%. From Fig. 8, it can be conformed that the experimental results match the theoretical and simulation waveforms.

IV. Accuracy Verification

In this section, the accuracy improvement of the proposed SSLC will first be verified.

As the previous discussion in Section II-C, the SSLC concept is proposed to improve the control accuracy. Fig. 9 shows the experimental results of the SSLC strategy under the full load operation. First, waveforms of V_{gs1}, V_o and I_o without the SSLC are shown in Fig. 9(a). In this case, the duty cycle is 30.5%, whereas V_o and I_o are measured as 43.1 V and 1.84 A, respectively. On the other hand, waveforms with the SSLC are shown in Fig. 9(b). In this scenario, the duty cycle will be 33.5%, whereas V_o and I_o are regulated as 47.3 V and 2.05 A, respectively. It should be noticed that under the full load operation, the theoretical V_o and I_o value should be 48 V and 2.083 A.

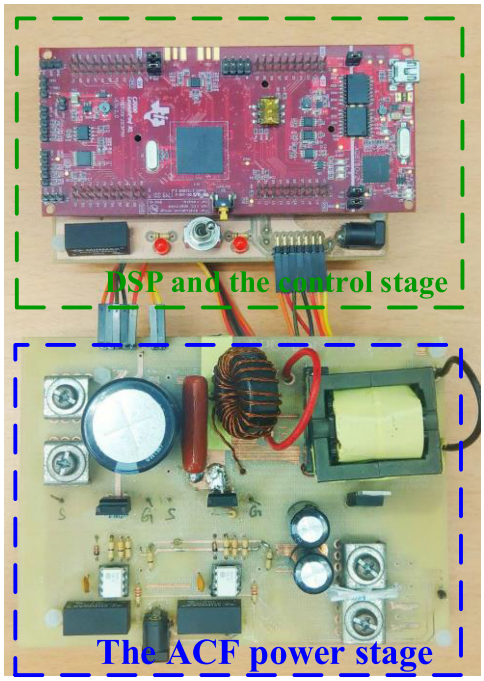

Fig. 7. Prototype circuit figure of the proposed ACF.

TABLE II
COMPARISON OF THE OUTPUT VOLTAGE ERROR

Output power	20%	40%	60%	80%	100%
Output voltage (Without SSLC)	47.2V	45.6 V	44.5 V	43.5 V	42.5 V
Output voltage (With SSLC)	47.9 V	47.8 V	47.5 V	47.4 V	47.3 V
Voltage error (Without SSLC)	1.67%	5%	7.29%	9.38%	11.5%
Voltage error (With SSLC)	0.02%	0.04%	1%	1.3%	1.5%

In order to further verify the performance of the SSLC, the accuracy and error comparisons will be presented with both output voltage and output current mode control. Table II and Fig. 10(a) illustrate the comparison results of the SSLC under the output voltage control in different load conditions. It can be seen that without the SSLC, the output voltage error will be increased from 1.67% to 11.5%. Therefore, the output voltage accuracy will be decreased from 98.33% to 88.54%. However, with the SSLC, the maximum error will be only 1.5%, whereas the voltage control accuracy can be over 98.5%.

On the other hand, Table III and Fig. 10(b) show the comparison results of the SSLC under the output current control in different load conditions. The results show that without the SSLC, the output current error will be increased from 3.85% to 11.7%. Consequently, the output current accuracy will be decreased from 96.15% to 88.3%. However, with the SSLC, the maximum error will be 1.6% while the current control accuracy will be over 98.4%.

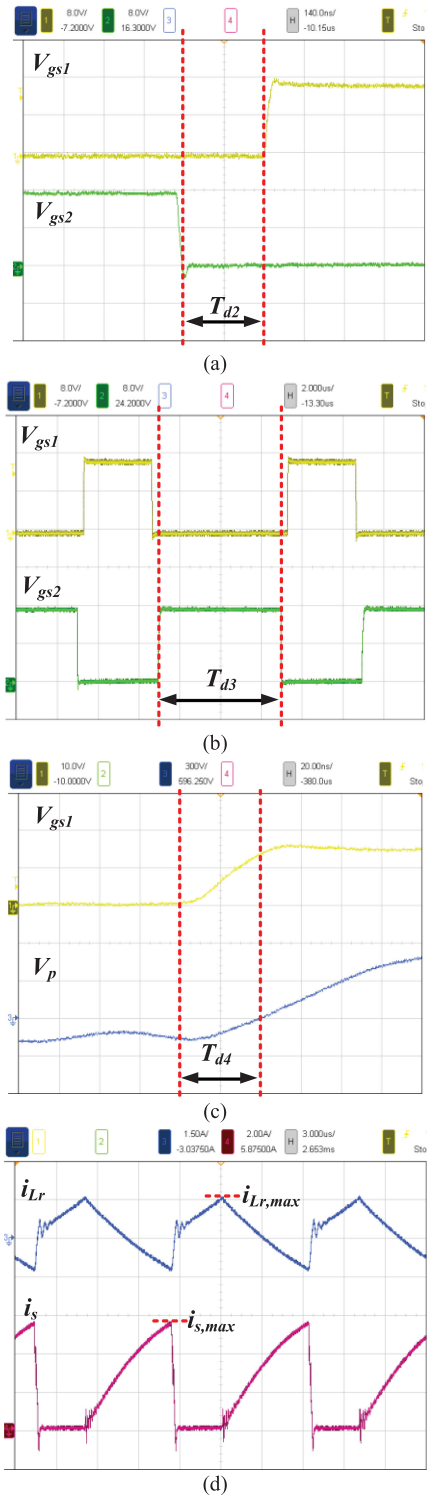

Fig. 8. Experimental waveforms of the proposed ACF converter. (a) V_{gs1}, V_{gs2}, and T_{d2}. (b) V_{gs1}, V_{gs2}, and T_{d3}. (c) V_{gs1}, V_p, and T_{d4}. (d) i_{Lr} and i_s.

From the above discussions, if the load is increased, the error will be increased and the accuracy will be decreased without the SSLC. However, with the developed SSLC strategy, the error can effectively be eliminated, whereas the accuracy will be improved in both voltage and current control.

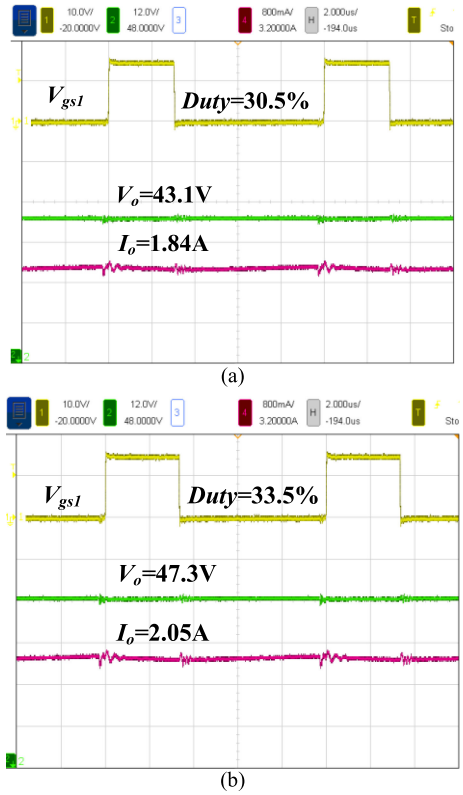

Fig. 9. Experimental comparison waveforms under the full load operation. (a) Without SSLC. (b) With SSLC.

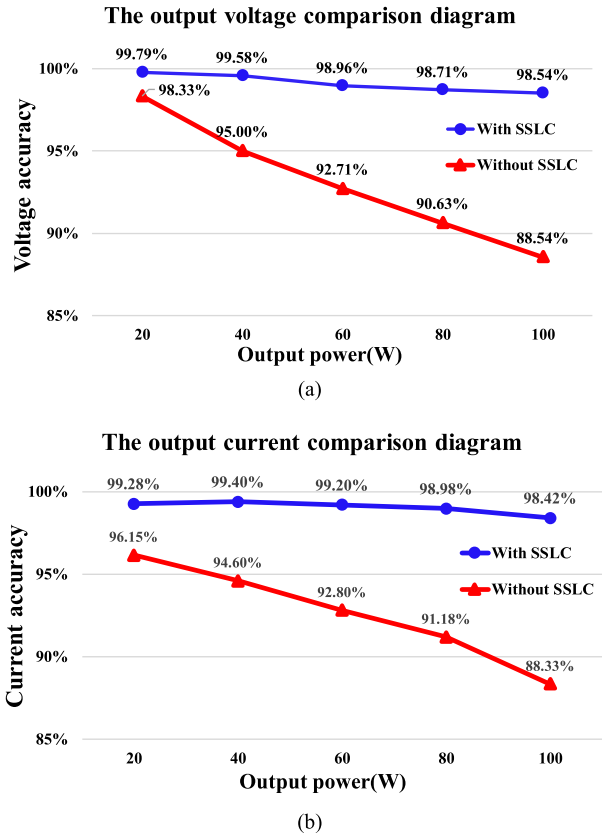

Fig. 10. Accuracy comparisons of the SSLC. (a) With the output voltage control. (b) With the output current control.

TABLE III
COMPARISON OF THE OUTPUT CURRENT ERROR

Output power	20%	40%	60%	80%	100%
Output current (Without SSLC)	0.4A	0.79A	1.16A	1.52A	1.84A
Output current (With SSLC)	0.41A	0.83A	1.24A	1.65A	2.05A
Current error (Without SSLC)	3.85%	5.4%	7.2%	8.82%	11.7%
Current error (With SSLC)	0.07%	0.06%	0.08%	1%	1.6%

V. CONCLUSION

In this article, a high-precision PSR strategy is proposed for the ACF converter. The theoretical analysis, operational principles and mathematical derivations of the proposed PSR are first revealed. The proposed method can be adopted for both CCM and DCM operation. In addition, both the output voltage and the output current control mode can be selected. A 100 W ACF prototype circuit is built, whereas the feasibility is verified via both simulation and experimental results.

Moreover, in order to decrease the control error as well as to improve the accuracy, a SSLC strategy is developed. The proposed PSR and SSLC concept can be realized via the DSP without adding extra circuit and components. Experimental results indicate that with the proposed SSLC, the control accuracy will be over 98.54% and 98.42% under the output voltage control mode and the output current control mode, respectively.

REFERENCES

[1] Y. Qin, Y. Yang, S. Li, Y. Huang, S. Tan, and S. Y. Hui, "A high efficiency DC/DC converter for high voltage gain high current applications," *IEEE J. Emerg. Sel. Topics Power Electron.*, vol. 8, no. 3, pp. 2812–2823, Sep. 2020.

[2] B. Yuan, J. Ying, W. T. Ng, X. Lai, and L. Zhang, "A high-voltage DC–DC buck converter with dynamic level shifter for bootstrapped high-side gate driver and diode emulator," *IEEE Trans. Power Electron.*, vol. 35, no. 7, pp. 7295–7304, Jul. 2020.

[3] K. Kim, J. Han, B. Lee, and G. Moon, "High-efficiency three-level DC–DC converter with reduced circulating current and rectifier voltage stress," *IEEE Trans. Power Electron.*, vol. 35, no. 3, pp. 2668–2679, Mar. 2020.

[4] H. Dong, X. Xie, and L. Zhang, "A new primary PWM control strategy for CCM synchronous rectification flyback converter," *IEEE Trans. Power Electron.*, vol. 35, no. 5, pp. 4457–4461, May 2020.

[5] S. Xu, Q. Shen, C. Wang, D. Ding, and W. Sun, "A digital control scheme for PSR flyback converter in CCM and DCM," *IEEE J. Emerg. Sel. Topics Power Electron.*, vol. 8, no. 3, pp. 2837–2849, Sep. 2020.

[6] V. Ravi and N. Lakshminarasamma, "Modeling, analysis, and implementation of high voltage low power flyback converter feeding resistive loads," *IEEE Trans. Ind. Appl.*, vol. 54, no. 5, pp. 4682–4695, Sep./Oct. 2018.

[7] J. Yang and H. Do, "Soft-switching dual-flyback DC–DC converter with improved efficiency and reduced output ripple current," *IEEE Trans. Ind. Electron.*, vol. 64, no. 5, pp. 3587–3594, May 2017.

[8] L. Xue and J. Zhang, "Highly efficient secondary-resonant active clamp flyback converter," *IEEE Trans. Ind. Electron.*, vol. 65, no. 2, pp. 1235–1243, Feb. 2018.

[9] R. Perrin, N. Quentin, B. Allard, C. Martin, and M. Ali, "High-temperature GaN active-clamp flyback converter with resonant operation mode," *IEEE J. Emerg. Sel. Topics Power Electron.*, vol. 4, no. 3, pp. 1077–1085, Sep. 2016.
[10] S. Xu *et al.*, "Sampled-data modeling for PCM and ZVS controlled critical conduction mode (CrCM) active clamp flyback (ACF) converter at variable switching frequency," *IEEE Trans. Circuits Syst. I, Reg. Papers*, vol. 67, no. 10, pp. 3588–3600, Oct. 2020.
[11] T. Liang, K. Chen, and J. Chen, "Primary side control for flyback converter operating in DCM and CCM," *IEEE Trans. Power Electron.*, vol. 33, no. 4, pp. 3604–3612, Apr. 2018.
[12] C. Wang, D. Sun, and W. Gu, "Stability analysis of constant current controlled primary-side regulation flyback converter," *IEEE J. Emerg. Sel. Topics Power Electron.*, doi: 10.1109/JESTPE.2020.3010347.
[13] H. Dong, X. Xie, and L. Zhang, "A new primary PWM control strategy for CCM synchronous rectification flyback converter," *IEEE Trans. Power Electron.*, vol. 35, no. 5, pp. 4457–4461, May 2020.
[14] S. Xu, Q. Shen, C. Wang, D. Ding, and W. Sun, "A digital control scheme for PSR flyback converter in CCM and DCM," *IEEE J. Emerg. Sel. Topics Power Electron.*, vol. 8, no. 3, pp. 2837–2849, Sep. 2020.
[15] C. Zhao, X. Xie, H. Dong, and S. Liu, "Improved synchronous rectifier driving strategy for primary-side regulated (PSR) flyback converter in light-load mode," *IEEE Trans. Power Electron.*, vol. 29, no. 12, pp. 6506–6517, Dec. 2014.
[16] Y. Li and Z. Zhu, "A constant current control scheme for primary-side controlled flyback controller operating in DCM and CCM," *IEEE Trans. Power Electron.*, vol. 35, no. 9, pp. 9462–9470, Sep. 2020.
[17] C. Wang, S. Xu, S. Lu, and W. Sun, "A low-cost constant current control method for DCM and CCM in digitally controlled primary-side regulation flyback converter," *IEEE J. Emerg. Sel. Topics Power Electron.*, vol. 6, no. 3, pp. 1483–1494, Sep. 2018.
[18] Y. Chen, C. Chang, and P. Yang, "A novel primary-side controlled universal-input AC–DC LED driver based on a source-driving control scheme," *IEEE Trans. Power Electron.*, vol. 30, no. 8, pp. 4327–4335, Aug. 2015.
[19] C. Wu, Y. Chen, and Y. Chen, "High-precision constant output current control for primary-side regulated flyback converters," in *Proc. 28th Annu. IEEE Appl. Power Electron. Conf. Expo.*, 2013, pp. 3092–3095.
[20] Y. Han, Q. Wu, Y. Li, and Z. Zhu, "Average inductor current measure and control strategy for multimode primary-side flyback converters," *IEEE Trans. Power Electron.*, vol. 35, no. 12, pp. 13096–13103, Dec. 2020.
[21] S. Xu, Q. Shen, C. Wang, D. Ding, and W. Sun, "A digital control scheme for PSR flyback converter in CCM and DCM," *IEEE J. Emerg. Sel. Topics Power Electron.*, vol. 8, no. 3, pp. 2837–2849, Sep. 2020.
[22] Z. Wang, X. Lai, and Q. Wu, "A PSR CC/CV flyback converter with accurate CC control and optimized CV regulation strategy," *IEEE Trans. Power Electron.*, vol. 32, no. 9, pp. 7045–7055, Sep. 2017.

Cheng-Yu Tang (Member, IEEE) received B.S degree in electrical engineering from the National Kaohsiung University of Applied Sciences, Kaohsiung, Taiwan, in 2010, and the M.S. degree in electrical engineering from the National Taipei University of Technology, Taipei, Taiwan, in 2012, and the Ph.D. degree in electrical engineering from the National Taiwan University, Taipei, Taiwan, in 2016.

He is currently an Associate Professor with the Department of Electrical Engineering, National Taipei University of Technology, Taipei, Taiwan. His research interests include switching power supplies, renewable energy systems and power flow control.

Wei-Zhen Lin received the B.S. and M.S. degrees in electrical engineering from the National Taipei University of Technology, Taipei, Taiwan, in 2019 and 2021.

He is currently the Electrical Design Senior Engineer with the Delta Electronics, Taoyuan, Taiwan. His research interests include digital control power converters and resonant converters.

Yu-Ching Tan received B.S degree in electrical engineering from National Ilan University, Ilan, Taiwan, in 2020. She is currently working toward the M.S. degree in electrical engineering from the National Taipei University of Technology, Taipei, Taiwan.

Her research interests include applications of switching power supplies, power electronics and resonant converters.